Computers and Electronics in Agriculture 191 (2021) 106514

Contents lists available at ScienceDirect

Computers and Electronics in Agriculture

journal homepage: www.elsevier.com/locate/compag

Estimation of leaf area index using inclined smartphone camera

Yonghua Qu [a,b,*], Zixin Wang [a,b], Jiali Shang [c], Jiangui Liu [c], Jie Zou [d]

[a] State Key Laboratory of Remote Sensing Science Jointly Sponsored by Beijing Normal University and Institute of Remote Sensing and Digital Earth of Chinese Academy of Sciences, Beijing 100875, China
[b] Beijing Engineering Research Center for Global Land Remote Sensing Products, Institute of Remote Sensing Science and Engineering in Faculty of Geographical Science of Beijing Normal University, Beijing 100875, China
[c] Ottawa Research and Development Centre, Agriculture and Agri-Food Canada, Ottawa, Ontario K1A 0C6, Canada
[d] The Academy of Digital China (Fujian), Fuzhou University, Fuzhou 350116, China

ARTICLE INFO

Keywords:
Leaf area index
Mean tilt angle
Smartphone camera
Inclined photography
Directional gap fraction

ABSTRACT

Measurements of leaf area index (LAI) are important for modeling microclimate in vegetation research. Among the instruments for measuring the LAI, smartphone cameras are becoming an attractive alternative to special LAI instruments. However, the narrow full field of view (FOV) of the common smartphones offer only an effective viewing zenith angle (VZA) of less than 35° when the camera is pointing straight up. To overcome this limitation, we propose a method to estimate LAI from an inclined smartphone camera that can enlarge the range of the sensor's effective VZA. With the directional gap fractions extracted from the images taken by the inclined smartphone camera, a curve matching algorithm is used to iteratively search for the simulated *G* functions, i.e. functions of mean tilt angle (MTA) and VZA. The MTAs corresponding to the matched *G* functions are selected as ancillary parameters to help calculate the LAI. The proposed method is validated using data collected over crops and trees by a LAI-2200 instrument and a Huawei Honor 7 smartphone. The results reveal that an inclination angle of 30° from zenith is superior to other angles of 0, 45 and 60°. A good agreement between the LAI measurements from the proposed method and those from the LAI-2200 supports the accurate estimation of MTAs. The success of the MTA estimates and thus LAI measurements is attributed to the enlarged VZA ranging from 4° to 60°, and this VZA is comparable with that of the LAI-2200 instrument. The attraction of the proposed method is that it does not rely on the empiric al *G* value or MTA, providing an affordable alternative to traditional commercial instruments. Future efforts can be directed to automatically capture images when the smartphone is inclined to the desired angle.

1. Introduction

The leaf is an important photosynthesis organ for most land vegetation. Leaf area index (LAI), defined as half of the total surface area per unit ground area (Chen and Black, 1992), is the quantitative representation of the ratio of leaf area corresponding to its vertical projection to the ground. LAI affects how incident photosynthetically active radiation is distributed on plant leaves, thus directly affecting plant productivity (Ross, 1981). The measurements of LAI can be achieved either directly from destructive plant harvest or indirectly by sensor-based method. Direct measurement is time- and labor-intensive since it requires outdoor manual collection of leaf samples and indoor measurements using a scanner, e.g., an LI-3000C Portable Leaf Area Meter (LI-COR, Lincoln, NE, USA), or the specific-leaf-area method (Chen et al., 1997). Indirect measurements, which in most cases rely on light-sensitive sensors to detect the transmitted light through the plant canopy, is more attractive for its convenience in fieldwork. Both methods have been reviewed in recent decades (Bréda, 2003; Jonckheere et al., 2004; Weiss et al., 2004; Welles, 1990). Recently, indirect optical methods were reviewed by Yan et al. (2019). A summary of the reviewed work shows that camera-based optical methods are one of the mainstream methods to carry out field LAI collection, taking advantage of their low cost and high availability.

The foundation of the camera-based method is to calculate the canopy gap fraction from a captured image and then transform gap fraction

* Corresponding author at: State Key Laboratory of Remote Sensing Science Jointly Sponsored by Beijing Normal University and Institute of Remote Sensing and Digital Earth of Chinese Academy of Sciences, Beijing 100875, China.
E-mail addresses: qyh@bnu.edu.cn (Y. Qu), 201821051081@mail.bnu.edu.cn (Z. Wang), jiali.shang@canada.ca (J. Shang), jiangui.liu@canada.ca (J. Liu), zoujie@fzu.edu.cn (J. Zou).

https://doi.org/10.1016/j.compag.2021.106514
Received 19 April 2021; Received in revised form 21 October 2021; Accepted 21 October 2021
Available online 8 November 2021

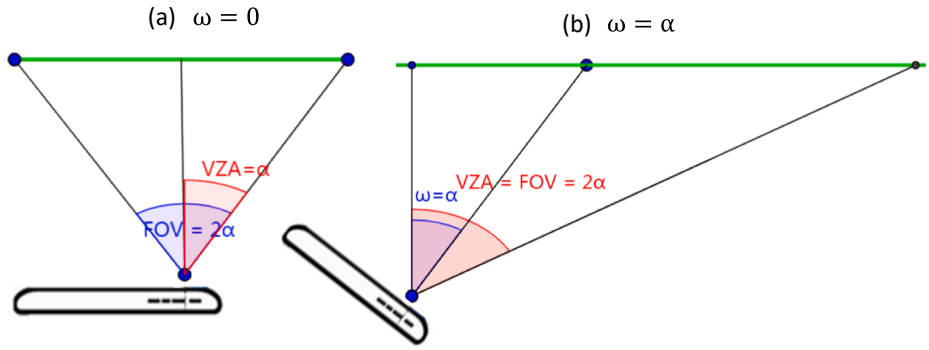

Fig. 1. Relation between camera field of viewing (FOV = 2α) and viewing zenith angle (VZA) of the pixels in a captured image. (a) Camera placed in horizontal mode where rotation angle $\omega = 0$ and VZA in [0, α]. (b) Camera rotated at a special angle, where $\omega = \alpha$ and VZA in [0, 2α].

into LAI by a Beer-Lambert law based model that states that

$$p(\theta) = \exp\left(-\frac{G(\theta)}{\cos(\theta)}L\right), \tag{1}$$

where θ is the viewing zenith angle (VZA), which can be derived from camera geometry, p is the gap fraction, which can be calculated from the classification of the canopy image, G is the projection of unit foliage area on the plane perpendicular to the viewing direction, and is a function of the leaf angle distribution (LAD) or MTA and VZA. Here, L is termed effective LAI or LAI_e in the literature (Nilson, 1971). It is assumed that leaves are spatially randomly distributed, and the clumping index is not considered (Chen and Cihlar, 1995). The LAI_e can be corrected by the clumping index to produce the true LAI (LAI_t). In this study, we focus on LAI_e instead of LAI_t because quantifying LAI_e using optical-based indirect methods is the first step to estimate LAI_t (Ryu et al., 2010a).

LAI can be calculated by solving Eq. (1) as

$$L = -\frac{\cos(\theta)}{G(\theta)}\ln(p(\theta)). \tag{2}$$

In Eqs. (1) and (2), there are two unknown free variables, i.e., L and G. Given L as the target variable, determination of G needs the knowledge of LAD or its derived value as MTA. Basically, rational assumptions or proper calculated values of the G are desired to accurately estimate the LAI.

A digital hemispherical (DHP) camera can produce images with a full field of viewing (FOV) of 180°; as a result, it is possible to obtain gap fraction as a function of zenith angle varying from 0 to 90° because the viewable range of the camera is related to the sensor's FOV. The CANEYE software (Weiss and Baret, 2017), which is widely used in processing DHP images to retrieve LAI, has implemented the above procedure to solve Eq. (2) by searching the optimized LAI and MTA in a simulated look-up table (LUT). Lang (1987) and the latest improved version (Gonsamo et al., 2018) estimate LAI from Eq. (2) with the help of Miller's integral (Miller, 1967) by the linear or robust regression method. However, the success of these solutions requires a wide range of VZAs that usually are resulted from hemispherical photo taken either by a fisheye lens with large FOVs of up to 180° (Chianucci and Cutini, 2013; Liu et al., 2013) or a common lens but a series of spherical panorama images (Vicent Agustí Ribas Costa, 2021).

Smartphone and digital cover photography cameras usually have a narrow FOV (approximately 70° in diagonal direction), which results in a half zenith angle bounded within 0–35° when the smartphone is held in horizontal layout (viewing the vertical upward direction). With such a limited zenith angle range, it is difficult to directly use the DHP method in this case to solve Eq. (2). As a result, assumptions of LAD or G should be made before LAI can be estimated. LAISmart (a LAI application using smartphone), which uses images captured in the vertical upward mode, assumes that LAD follows a spherical distribution, and in this mode, the G value is a constant of 0.5 (Qu et al., 2017, 2016). PocketLAI, which calculates LAI from images captured at a 57.5° view angle, takes the G value of 0.5 in this so-called hinge angle (Confalonieri et al., 2013). Both LAISmart and PocketLAI simplify the effort to solve Eq. (2) on the basis of their assumptions. However, large uncertainty or bias could exist in the estimated LAI when the assumption of G is violated to its real situation. For example, the method of 57.5° requires the gap fraction measured strictly at the VZA of 57.5° (Wilson, 1963), rather than the mean value of an image with a large range of VZA (Confalonieri et al., 2014). For the method of LAISmart, there are situations when the assumption of spherical LAD mode is violated in field situations (Pisek et al., 2013; Zou et al., 2020). Fang et al (2018) carried out a comparison of LAI measurements from several optical instruments. They reported that compared with reference values of the LAI-2200, the relative errors for the LAISmart estimates were within 20–30% and for PocketLAI they were larger than 40%.

From the model of calculating LAI in Eq. (2), it is inferred that the overestimation of the gap fraction and the unrealistic assumption on G are the two primary factors contributing to the LAI uncertainty of smartphone cameras. The former can be easily relieved by an improved image classification algorithm, as has been done by Fang et al (2018). However, to the best of our knowledge, the latter issue of calculating G or its derivation as MTA in smartphone-based methods has not yet been investigated widely. To date, there is only one similar study to measure the leaf angle using smartphones (Qi et al., 2019). However, Qi's method is based on point clouds and a convolutional neural network (CNN) classification to extract leaf boundaries. Although agreement with manual measurement was found in their work, the need for multiple images to generate point clouds and the time-consuming training process of CNNs might restrict their implementation in smartphone computing environments. Therefore, regarding the issue of measuring LAI from gap fraction data, the lack of a proper G or MTA for realistic vegetation canopies limits the performance of the retrieved LAI. Digital photography is proven to be a rapid, noncontact and accurate method for MTA estimation (Pisek et al., 2011; Raabe et al., 2015; Ryu et al., 2010b; Zou et al., 2014). However, as indicated by the results of Raabe et al (2015), this method is difficult to automate because their methods involve manual measurements of the leaf angle with the help of professional image processing software (e.g., ImageJ, 2020).

As mentioned earlier, directional gap fractions on multiple angles are needed to model LAIs and estimate MTAs from smartphone camera images. It is assumed that once the MTA and the G values are properly calculated, the LAI estimation performance will be improved. We assume that it is possible to extract the directional gap fraction from smartphone cameras by a dedicated design of an image capturing strategy. With this assumption, when vegetation images are captured using inclined smartphones, the range of VZA will be enlarged compared with the traditional vertical upward-looking mode of imaging.

In this work, we explore the information in images captured by

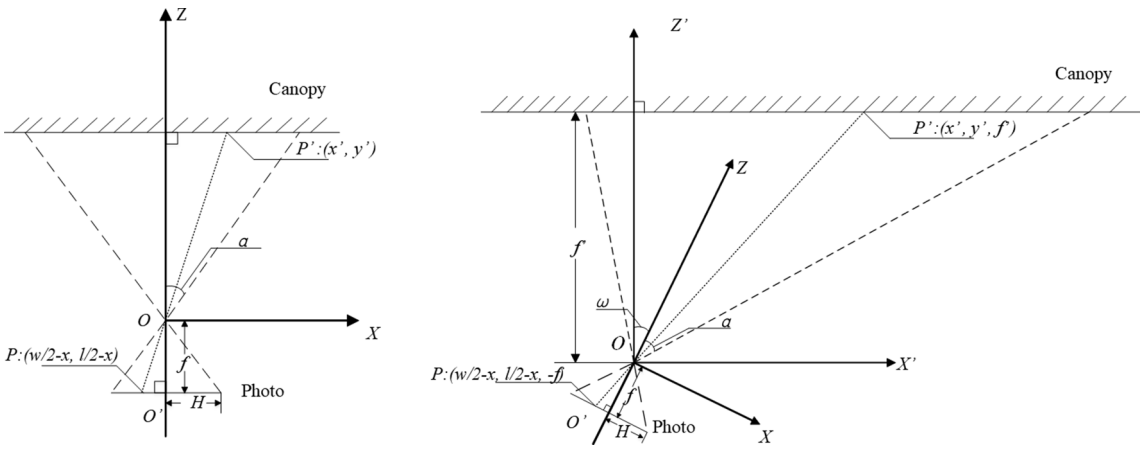

Fig. 2. Coordinate system of camera location. (a) Camera is placed in horizontal mode. (b) Camera is inclined at the angle of ω.

inclined smartphone cameras, which have a narrow FOV range. The primary objective is to estimate plant LAI using consumer-grade smartphones. The secondary objective is to identify factors that might affect the performance of the estimated LAI and the efficiency of the measurement of the LAI using the proposed method. The above objectives will be fulfilled by analyzing a series of images collected in plots using a smartphone with different inclination angles.

2. Methodology

2.1. Viewing zenith angle of the image for an inclined smartphone camera

When the smartphone camera is placed on the level plane (Fig. 1a) and its viewing direction is in upward-looking mode or its principle optical axis (POA) is in the vertical direction, the maximum of the VZA of the image pixels is half of the full FOV. When a camera has an FOV of 70°, which is the common configuration for most consumer-grade smartphone cameras, its VZA is limited to the range of 0–35°, as has been investigated by Qu et al (2016) and further confirmed by the indoor experiment (Appendix C). In this mode, pixels are symmetrically arranged around the POA on the azimuth plane. As a result, the symmetric relation of pixels around the sensor's POA causes a narrow effective range of VZA in the captured image.

However, if the smartphone camera is placed inclined against the vertical axes at an angle of ω, then the symmetry of pixels around the zenith line will be changed (Fig. 1b). As a special case, for example, if the smartphone camera is inclined at an angle of its half FOV, then the minimum VZA is zero and the maximum is its upper boundary of the FOV angle. We can see that the limitation of the narrow VZA range can be solved by a simple inclination of the smartphone camera.

The zenith angle of every pixel can be calculated using the parameters of the smartphone camera, e.g., the resolution of the pixel number of an image and the rotation angle ω. We describe the location of the smartphone in 2-D space using the coordination system as illustrated in Fig. 2.

In Fig. 2(a), the point of O is the original centers of the coordinate system, X is the planes of the camera, f is the distance between the camera center and the photo plane, and H is the diagonal of the photo, which has $w \times l$ pixels in width and length, respectively. In Fig. 2(b), all the symbols with superscripts of a single quotation are the rotated points corresponding to those of Fig. 2(a) when the original coordinate system is rotated at an angle of ω.

The simplest case is in the horizontal mode of $\omega = 0$. In this mode, we calculate the zenith angle of pixels using the following steps.

With the known the image width (w) and length (l) in pixel units, then, the half-length of diagonal H is calculated as

$$2H = \sqrt{w^2 + l^2}. \tag{3}$$

Let the angle of the FOV be 2α; then, the distance of the camera focus center to the photo plane (d) can be calculated as

$$d = \frac{H}{2\tan\alpha}. \tag{4}$$

Therefore, the following equation holds to calculate the zenith angle (θ) corresponding to any pixel location (x, y) on the assumption that the VZA of any pixel is linear to its distance to the centroid of the image (Rao, 2021).

$$\tan\theta = d^{-1}\sqrt{\left(x - \frac{w}{2}\right)^2 + \left(y - \frac{l}{2}\right)^2}. \tag{5}$$

To evaluate the case of a smartphone inclined at an angle of ω, the following projection equation is used to calculate the pixel coordinate (x', y', d') that corresponds to the original level plane location (x, y, d) (Knisley, 2001):

$$(x', y', d') = \left(x - \frac{w}{2}, y - \frac{l}{2}, d\right)\begin{pmatrix} 1 & 0 & 0 \\ 0 & \cos\omega & -\sin\omega \\ 0 & \sin\omega & \cos\omega \end{pmatrix} \tag{6}$$

With the new coordinates of (x', y', d'), the zenith angle of any pixel can then be calculated using Eq. (7) with the same assumption of linear projection of camera image as the calculation in Eq. (5) (Rao, 2021).

$$\cos\theta = \frac{d'}{\sqrt{(x')^2 + (y')^2 + (d')^2}}. \tag{7}$$

2.2. Calculation of the G function from directional gap fractions

2.2.1. G function model and its shape

In theory, the G function is the product of the extinction coefficient (k) and the cosine of VZA (θ),

$$G(\theta) = k(\theta)\cos\theta. \tag{8}$$

According to the ellipsoid model of LAD proposed by Campbell (1986), $k(\theta)$ can be further modeled as

$$k(\theta) = \frac{(\chi^2 + tan^2\theta)^2}{1.47 + 0.45\chi + 0.1223\chi^2 - 0.013\chi^3 + 0.000509\chi^4}, \tag{9}$$

where χ is the ratio of vertical to horizontal projections of canopy elements and θ is the sensor viewing zenith angle.

The χ corresponding to a given MTA can be computed as Eq. (10) according to Campbell (1990),

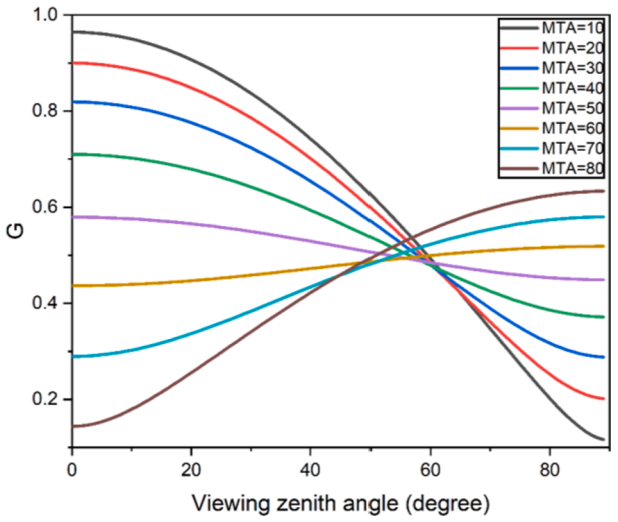

Fig. 3. Simulated G values varying with viewing zenith angles for different mean tilt angles.

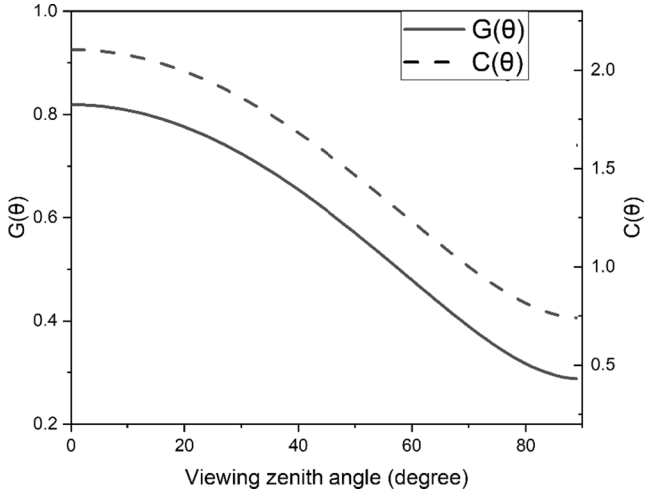

Fig. 4. Sketch illustrating the concept of Eq. (14), where the contact number function C(θ) is parallel to G(θ) when they are normalized by a certain algorithm.

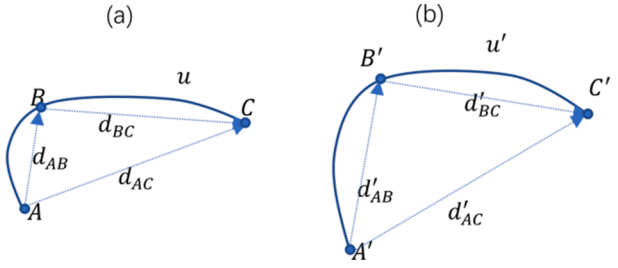

Fig. 5. Diagram illustrating the concept of the coefficient of discriminability. (a) Ordered points A, B, C in curve u and distance between the points d_{AB}, d_{BC}, d_{AC}. (b) Curve u' and points and distance corresponding to those in (a).

$$\chi = -3 + \left(\frac{MTA}{9.65}\right)^{-0.6061}. \tag{10}$$

By combining Eqs. (8)–(10), G values for different MTAs can be calculated, and Fig. 3 depicts the shapes of the G function when MTA varies from 10° to 80°.

2.2.2. Contact number and its relation with the G function

Eq. (2) can be transformed as

$$-\cos\theta \ln(p(\theta)) = L \times G(\theta). \tag{11}$$

Let the left part be $C(\theta)$, i.e.,

$$C(\theta) = -\cos\theta \ln(p(\theta)), \tag{12}$$

then, Eq. (11) can be rewritten as

$$C(\theta) = L \times G(\theta), \tag{13}$$

where $C(\theta)$ is defined as the averaged contact number in direction θ, and it is representative of the projection area of the total leaf area in the perpendicular plane to the viewing direction.

For a canopy scene captured by an image, LAI is a constant value to be solved. Therefore, the following equation can be derived according to Eq. (13)

$$C(\theta) \propto G(\theta), \tag{14}$$

where the symbol $\propto$ denotes that the observed value of $C(\theta)$ is proportional to the value of $G(\theta)$. This deduction implies that the shape of the observed $C(\theta)$ is similar to the shape of its $G(\theta)$ except that $G(\theta)$ is scaled by a positive factor. Specifically, for the ideal situation, the two curves might be parallel in 2-D space if their shapes are normalized by a certain algorithm. This concept can be illustrated using the following sketch plot (Fig. 4).

2.2.3. Matching the G function using measured gap fractions

The shape similarity of $C(\theta)$ derived from the measured directional gap fractions in Eq. (12) to $G(\theta)$ provides an opportunity to find the desired $G(\theta)$ by matching the shape of $C(\theta)$ with the theoretical $G(\theta)$. Specifically, we iteratively search the curve of $G(\theta)$ in the simulated theoretical curve inventory, which is produced using Eq. (8) - (10) with the input variables in the list of leaf MTAs (Fig. 3). Finally, the $G(\theta)$ that has minimum discriminability (or most similarity) with the observed C (θ) is selected as the optimized result of target $G(\theta)$.

As described in Eq. (13), $C(\theta)$ is the product of $G(\theta)$ and a positive scale factor (LAI). Therefore, the desired algorithm for describing the discriminability of their shapes should normalize their shapes, or the algorithm should be capable of scaling invariance with different shapes. A normalized distance of corner points (NDCP) matching algorithm (Zhang et al., 2009) is selected to match $C(\theta)$ with $G(\theta)$. In this algorithm, the difference between two curves is described by an index calculated as the coefficient of discriminability (COD). To calculate the COD, a curve is assumed to contain a series of ordered corner points (Fig. 5), and then a matrix composed of elements of the distance between all the points can be calculated. To eliminate the scale factor of the curve, the distances are normalized by the maximum among all the distance values of one curve. For example, for a curve u in Fig. 5a, its normalized distance D_u is calculated as

$$D_u = \begin{bmatrix} \frac{d_{AB}}{d_{AC}} \\ \frac{d_{BC}}{d_{AC}} \\ \frac{d_{AC}}{d_{AC}} \end{bmatrix}, \tag{15}$$

where symbols d_{AB}, d_{BC}, d_{AC} are the distance between points of their subscript.

In this manner, the normalized distance $D_{u'}$ for the curve u' (Fig. 5b) can be calculated as

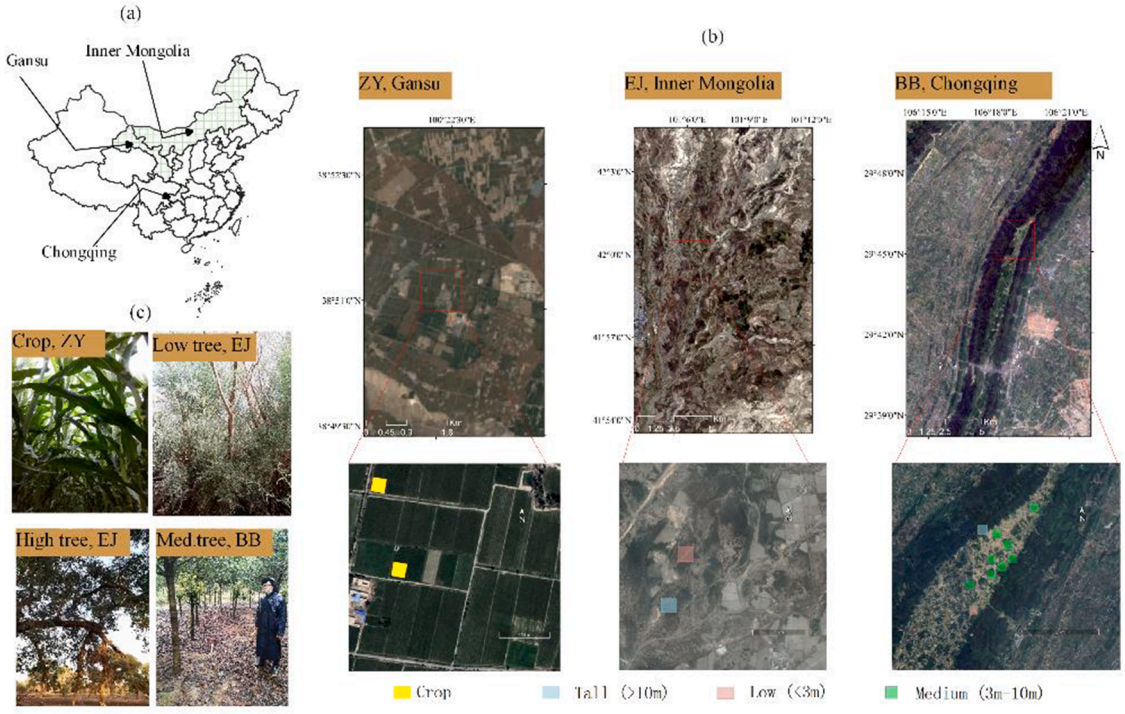

Fig. 6. Illustrations for field work regions. (a) Three regions located in China (green hatches indicate three provinces where field work was conducted). (b) Plot locations in the Google Earth image, where Zhangye (ZY), Ejin (EJ), and Beibei (BB) are arranged from left to right, and colored squares are the plots with different types and heights. (c) Example vegetation images in the three regions.

Table 1
Vegetation groups.

Groups (height)	Species	Regions
Crop	*Zea mays*	ZY
Tall (>10 m)	*Populus euphratica*; *Garcinia mangostana*	EJ and BB
Low (<3 m)	*Tamarix chinensis*; *Camellia petelotii*; *Alsophila metteniana*	EJ and BB
Medium (3–10 m)	*Osmanthus fragrans*; *Citrus maxima*; *Citrus reticulata*	BB

$$D_{u'} = \begin{bmatrix} \frac{d_{A'B'}}{d_{A'C'}} \\ \frac{d_{B'C'}}{d_{A'C'}} \\ \frac{d_{A'C'}}{d_{A'C'}} \end{bmatrix} \tag{16}$$

The ratio of all the elements in the normalized distance matrixes of two curves is called the discrimination matrix (DM). In this example, the DM of the two curves is composed of 3×3 elements that are derived from the ratio of elements of Eqs. (15) and (16).

As a result, the sum of all the element values in DM is calculated as COD. A larger COD indicates a greater difference between two curves and vice versa. It should be noted that the COD is negative when the two vectors are in opposite directions. A detailed computation algorithm and its source code on the COD can be found in Appendix A.

2.3. Estimation of leaf area index and mean tilt angle

For individual RGB images, directional gap fractions can be calculated by segmenting the original pixels into sky and leaf classes using the Otsu threshold method on the blue band (Otsu, 1979; Qu et al., 2016). Then, the contact number on different VZAs from Eq. (12) will be used to match the G function by minimizing the discrimination index of Eq. (A10) in Appendix A. Given the optimization of the G function in one image, the canopy MTA corresponding to the G function (Fig. 3) is determined. In a plot where more than one images are captured by a smartphone, the final MTA of this plot is the averaged MTA from all the available images. We take the average value as the plot's MTA under the assumption that at the plot scale, plants share a unique leaf angle distribution (Qu et al., 2020). As a result, MTA averaged from many images will represent the whole population. The averaged MTA will be used to calculate the LAI of the individual image by Eqs. (10), (9), (8) and Eq. (2). As conducted on the MTA plot, the averaged LAI of all the images in one plot is taken as the plot LAI.

3. Experimental data

Field data were collected from three regions in China (Fig. 6a), i.e., an agricultural region in Zhangye city (ZY), Gansu Province, a desert forest in Ejin Banner (EJ), Inner Mongolia, and a natural forest reserve in Beibei (BB) District Chongqing city (left to right panels in Fig. 6b). The three regions have very different climate conditions. The ZY region is located in the middle reaches of the Heihe River, and it is characterized as an arid and semiarid area with an annual precipitation of approximately 130 mm, so agricultural water depends heavily on irrigation from the Heihe River, the second largest inland river in China. In the ZY region, two plots of maize crop (*Zea mays*) fields were selected (upper left inset in Fig. 6c), and they were measured on three dates, July 8, July 15 and July 22, 2020. The EJ region is also in the Heihe River watershed; however, unlike the ZY region, which is in the middle reaches, the EJ region is in the lower reaches. With decreased surface runoff and very low annual precipitation of approximately 35 mm, EJ is an extremely arid desert area. The forest in the EJ region is dominated by trees of poplar (*Populus euphratica*) (lower left inset in Fig. 6c) and shrubs of tamarix (*Tamarix chinensis*) (upper right inset in Fig. 6c). Two plots were designed in the EJ region, and they were measured on two dates, July 13 and July 24, 2020. The BB in the Chongqing region benefits from abundant rainfall of annual precipitation larger than 1000 mm, so

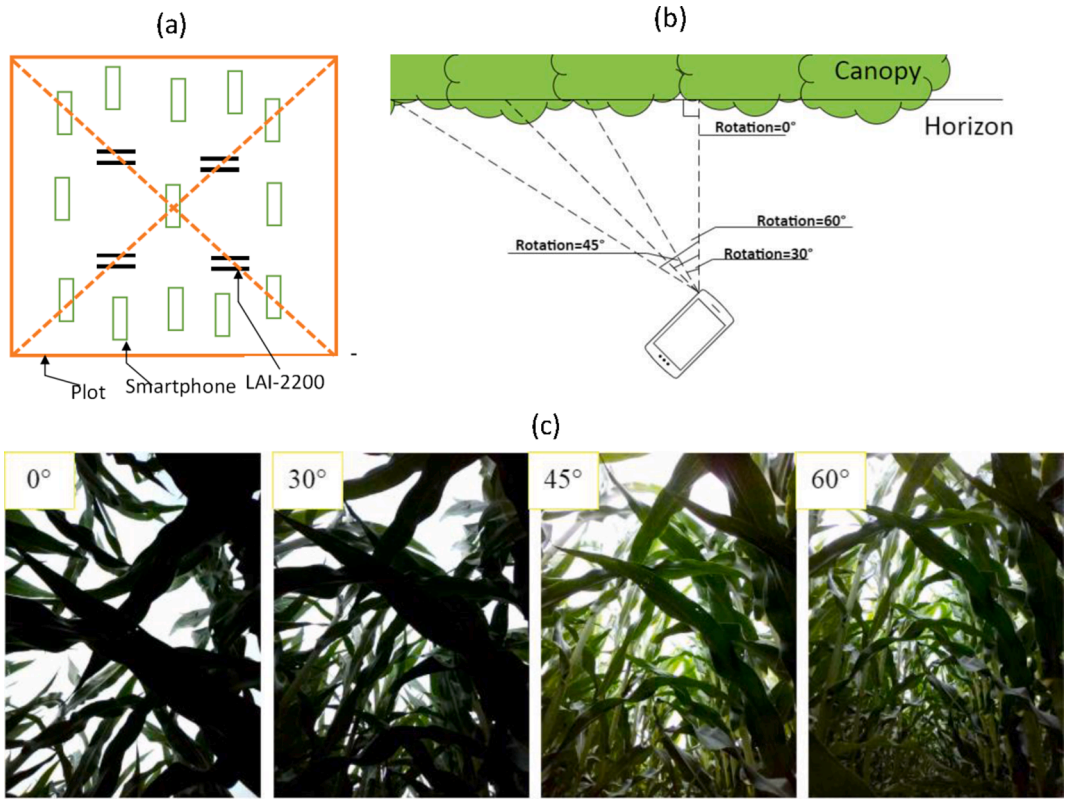

Fig. 7. Protocol of LAI-2200 (black double lines) and smartphone (green squares) measurements in one plot with the size of 30 × 30 m^2 in (a), where for every point, four smartphone images were taken at four inclined angles as indicated as (b), and four example images taken at four angles were shown in (c).

diverse plant species are found in this region. We measured the dominant vegetation type in this region, i.e., May flower trees (*Osmanthus fragrans*) (lower right inset in Fig. 6c), two types of citrus trees (*Citrus maxima* and *Citrus reticulata*), bamboo trees (*Garcinia mangostana*), and mixed forest comprised of camphor trees (*Cinnamomum camphora*) and May flower trees (*Osmanthus fragrans*). Ten plots were designed in the BB region, and they were measured on dates from October 19 to October 22, 2020. The trees in the EJ and BB regions were cataloged by their height into three groups (Table 1).

In these plots, a smartphone (Huawei Honor 7 model) was used to collect canopy images and it is held to look upward from the bottom of the canopy, i.e., with the presence of leaves and sky in the image. The smartphone was set at different heights above ground depending on the height of the vegetation to be measured. Specifically, for low trees and crops, the smartphone was held about 5 cm above the ground to ensure that all the vegetation organs were imaged by the camera. In this mode, the operator had to bend down, while for the medium or tall trees, the operator held the smartphone at the height about 1.0 m above the ground. In one plot, approximate 13 points surrounding the LAI-2200 point were selected (Fig. 7). The locations of the points were arranged surrounding the LAI-2200 points to ensure the output of the two methods are comparable (Fig. 7a). At each point, images were taken with the camera inclined at four inclination angles, i.e., $\omega = 0^{\circ}, 30^{\circ}, 45^{\circ}, 60^{\circ}$ as shown in Fig. 7b. These angles were selected because in the case of 0°, the image has a maximum overlaying VZA around the image center, and a minimum effective VZA will be observed, and from angle of 30°, which is near half of the FOV of the smartphone camera, the overlaying VZA will be deceased with an increased inclination angle (see Fig. 1 and Fig. 2). The LAISmart app installed on a smartphone was used to fulfill the above image taking work. The inclined angles were measured by the smartphone built-in gyro sensor and were read in real time from the screen. It should be noted that, in real field environment, it was hard to keep the smartphone fixed at the designed angles (i.e., $0^{\circ}, 30^{\circ}, 45^{\circ}, 60^{\circ}$) because the smartphone was hand-held by an operator without a fixed support. To reduce the uncertainty caused by the inclination angle, we triggered the camera only when the inclination angle was in the range of target angle ±2°. A smartphone front camera with a pixel resolution of 720 × 960 was used in this mode because it is convenient to touch the screen and read the output of the app. As an example, we provide four images taken at four angles in Fig. 7c.

When measured with the LAI-2200 instrument, in every plot, four points along the diagonal of the plot were selected to collect reference LAI and MTA (Fig. 7a). The LAI-2200 needs the below- and above-canopy radiance to calculate light transmittance; for the below-canopy measurement, the LAI-2200 was held level at the same height as to smartphone. For the above measurement, since the LAI-2200 has a hemispherical viewing angle and needs a large open space to avoid shading from the trees, two protocols are designed for different vegetation groups according to the vegetation height. For crops, the LAI-2200 instrument was held above the top of the canopy to avoid the vegetation canopy obscuring the sensor. For the trees, according to the manual of the device, a large open space with a size at least 3 times the tree height was selected. For crop plots, since the canopy structure is relatively homogenous, the sensor of the LAI-2200 instrument was covered by a cap of 180° to prevent the operator from being viewed. For the other plots with relatively heterogeneous vegetation, a cap of 270° was used to prevent surrounding trees from being in the sensor's field of view.

Both smartphone and LAI-2200 need diffused light environment, so we measured data at dawn or twilight time or in cloudy conditions.

For comparison, plot-scale results of LAI and MTA derived from LAI-2200 and our method are produced. The coefficient of determination (R^2) and the root-mean-square error (RMSE) are used to present the accuracy and the relationship between the estimated and measured reference using the following equations:

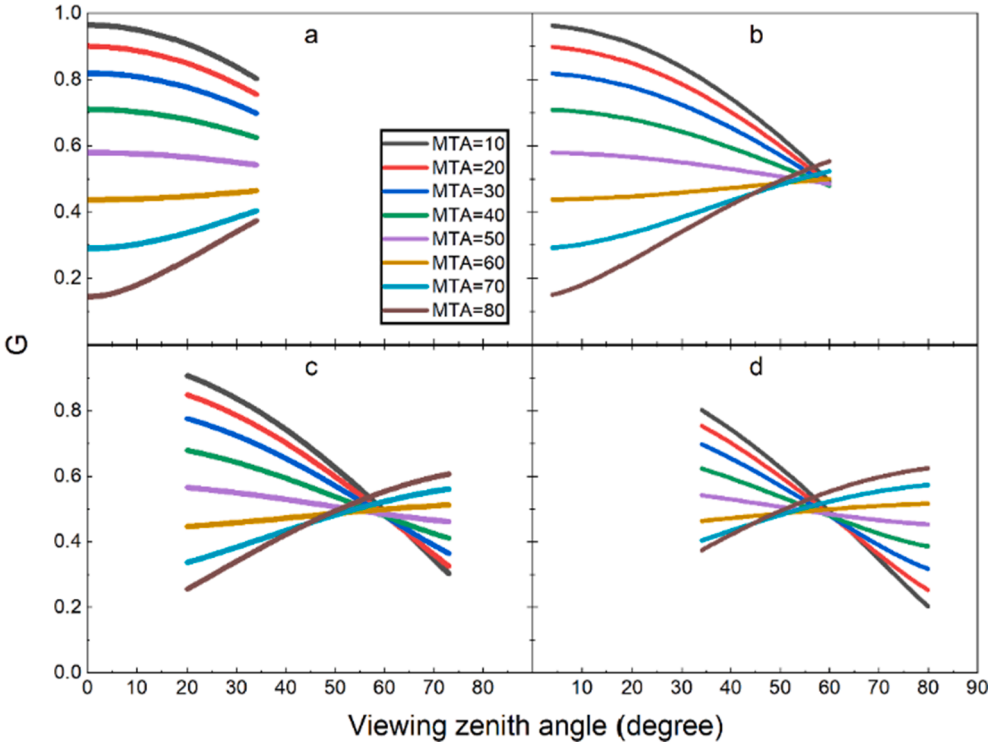

Fig. 8. Simulated truncated G function shapes in smartphone inclined mode. (a), (b), (c), and (d) illustrate the results when smartphones are inclined at 0°, 30°, 45° and 60°, respectively, where different colors represent leaf mean tilt angles ranging from 10° to 80°.

Table 2
Viewing zenith angles varying with camera inclined angles.

Inclined angle (°)	Lower boundary (°)	Upper boundary (°)	Range (°)
0	0	35	35
30	4	60	56
45	20	73	53
60	34	80	46

$$RMSE = \sqrt{\frac{1}{n}\sum_{i=1}^{n}(\widehat{y_i} - y_i)}, \tag{17}$$

$$R^2 = \frac{\sum_{i=1}^{n}(\widehat{y_i} - \overline{y})^2}{\sum_{i=1}^{n}(y_i - \overline{y})^2}, \tag{18}$$

where n is number of data points, $\widehat{y_i}$ and y_i are the estimated and reference LAI respectively, and $\overline{y}$ is the mean value of reference LAI.

4. Results and discussion

4.1. Truncated G function for different inclined angles

For the smartphone camera with a narrow FOV, when it is inclined off zenith angles, the boundary of camera VZA is varied accordingly, as indicated in Fig. 8. When the inclination angle is smaller than half the FOV angle (Fig. 8a), in the captured images, the lower boundary of VZA is kept at a fixed zenithal zero angle, which means that the canopy around a VZA of zero will be observed in these situations. When the inclination angle reaches the points outside of the half FOV (Fig. 8b–d), the zenithal zero angle will disappear, but the upper boundary of the VZA increases to approximately 80°. The above dynamic range of camera VZA varying with inclination angles is illustrated in Table 2.

Compared with the theoretical model of the *G* function in Fig. 3, only a partial *G* function shape rather than a full shape can be observed in the inclined smartphone camera (Fig. 8). Basically, estimating LAI with smartphone images using Eq. (2) is first inferring the full *G* function using a partial zenith observation, as shown in Fig. 8. The greatest difficulty from 'partial' to 'full' is selecting the optimized inclination angle at which the observed partial *G* function shapes of different MTAs have the largest difference or discriminability.

Using the discriminability equation of Eq. (A10) in Appendix A, we calculate the discriminability matrix as shown in Fig. 9 and we delineate the maximum values with yellow lines in every row that correspond to different leaf MTAs in Fig. 8. It should be noted that the negative values in the discrimination matrix represent the shapes of the *G* function of the two MTAs having opposite directions; for example, the *G* directions of MTA = 10 and MTA = 80 in Fig. 8. Undoubtedly, little difficulty occurs in differentiating shapes with totally different directions, so we focus on the situation where the shapes have the same directions that have positive values in Fig. 9.

From Fig. 9, it is easy to find that, in general, lower discrimination values are observed in the situation when the camera is kept in the horizontal mode (Fig. 9a), and increasing the inclined angle leads to a larger discrimination value, as indicated in Fig. 9b–d, which is further quantitatively manifested by the yellow outlines in Fig. 9a–d and illustrated by their sum values in Fig. 10. These results mean that when the camera is inclined at 30°, it is the easiest mode to infer the G function because this mode has the largest discrimination among all situations (Fig. 10).

As an example, we take the measurements from one point where the MTA reported by LAI-2200 is 60° to demonstrate the relationship between contact number C(θ) and the truncated G(θ). In this example, the calculated VZAs of four inclination modes lie in the ranges indicated in Table 2, and when the smartphone is inclined at 30°, the measured C(θ) has the smallest discrimination (largest similarity) with the modeled G when MTA is 60° (Fig. 11).

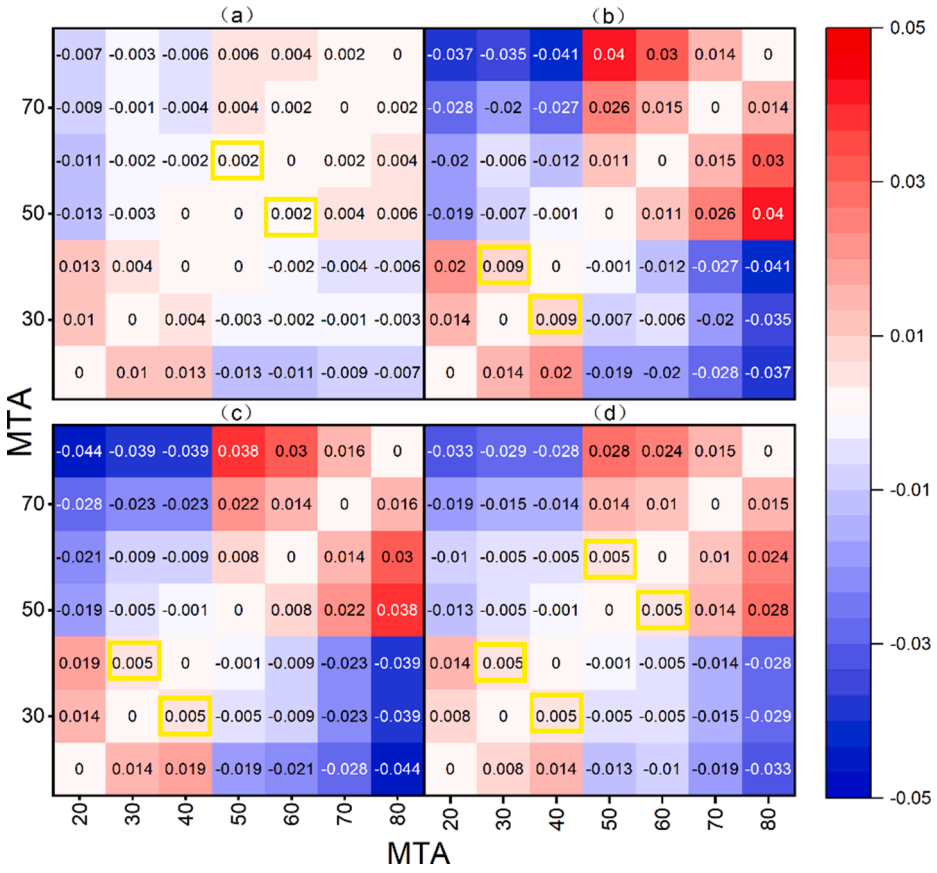

Fig. 9. Discriminability of G function shapes of different mean tile angles (MTAs) for inclined smartphones. (a)–(d) are the results when the smartphone is inclined at angles of 0°, 30°, 45° and 60°, respectively.

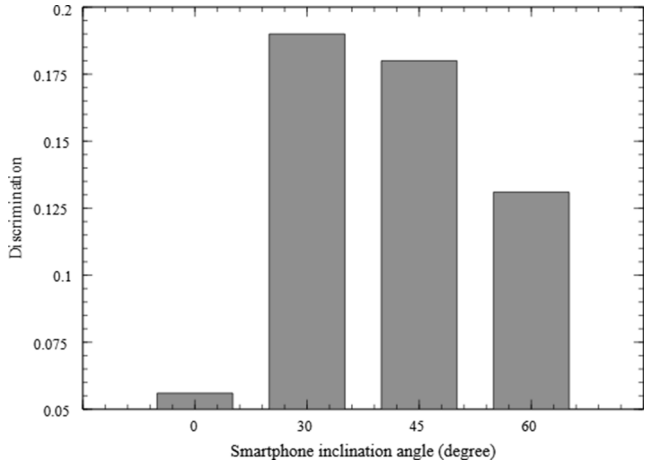

Fig. 10. Sum of the maximum discrimination value of all leaf mean tilt angles for different smartphone inclination angles.

4.2. Estimated mean tilt angle

The *G* function and its derivation as MTA are the first output of this proposed method, and we compare the derived MTA with those measured by LAI-2200 in Fig. 12. As expected after inspecting the discrimination of *G* functions in Fig. 10, when the smartphone is inclined at 30°, the output of MTA is superior to all other modes with the lowest RMSE of 8.23 and highest R^2 of 0.89 (Fig. 12b). In the other modes of 0°, 45° and 60° (Fig. 12a, c and d), no apparent difference in the MTA performance was observed, with RMSEs ranging from 16° to near 19° and a stable R^2 of approximately 0.40.

When the plot MTA is averaged by vegetation types, it is found that for a certain inclination angle, the performance of estimated MTA is stable on different vegetation types (Fig. 13); however, an inclination of 30° has the best performance, and in this case, absolute errors range from 5° to 8° for the four vegetation types. This result means that our proposed method is applicable to a wide range of vegetation types, e.g., from crops to trees of different heights.

Combining the results of Fig. 12 and Fig. 13, we find that, in most cases, our proposed method slightly overestimates the LAI-2200 MTA, and for the best result in the inclination of the 30° mode, a mean positive bias of 7° is observed in Fig. 13b. This result is unlike the result of Zou (Zou et al., 2014), who reported that LAI-2000 overestimated photographic measurements. Although the nonrandom distribution of leaves and diffusive light are considered the main sources of the bias of LAI-2200 and photographic methods, as suggested by the reviewer (Anonymous, 2015) of Zou's article, there is still not enough evidence to support these conclusions. Even in this case, in terms of the magnitude of the overestimation, its uncertainty is comparable to the photographic method reported by previous work (Raabe et al., 2015). However, automated estimation of MTA in this method means no extra manual work is needed, and as a time-saving method, it has the potential to be implemented in conducting efficient field work involving both LAI and MTA.

4.3. Estimated leaf area index

For the performance of LAI estimation at four inclination angles (Fig. 14), it is not surprising that with the help of accurate estimation of leaf MTA in the inclination of 30° mode, it produces higher quality LAI in this mode (Fig. 14b). Specifically, compared with LAI-2200, in this

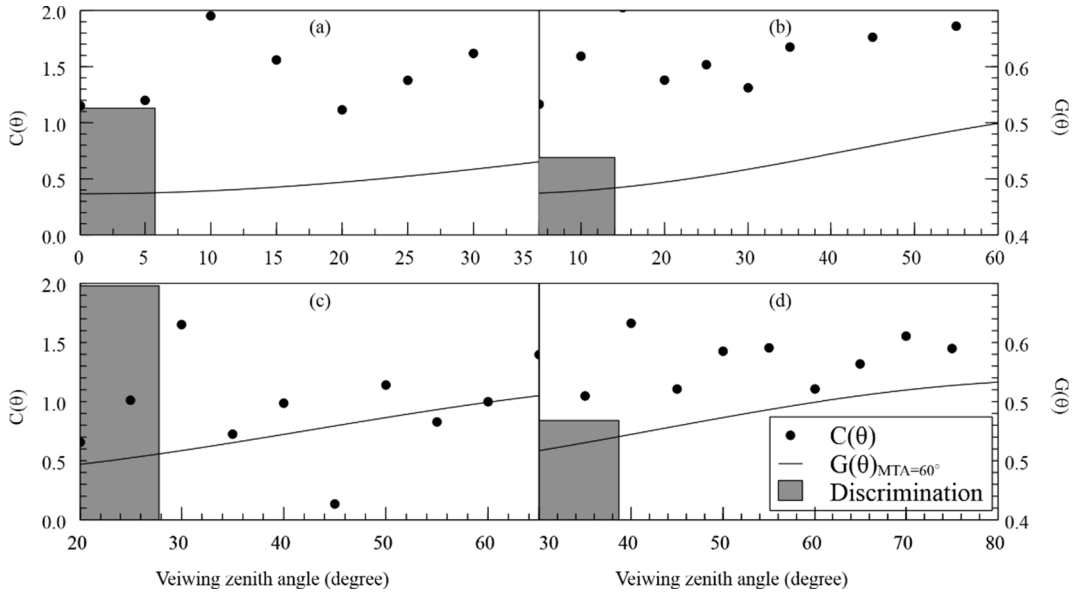

Fig. 11. Examples of measured contact number and the truncated *G* function, where the discrimination index is indicated by the grey bar. Panels (a)–(d) are the results from inclination 0°, 30°, 45°, and 60° respectively.

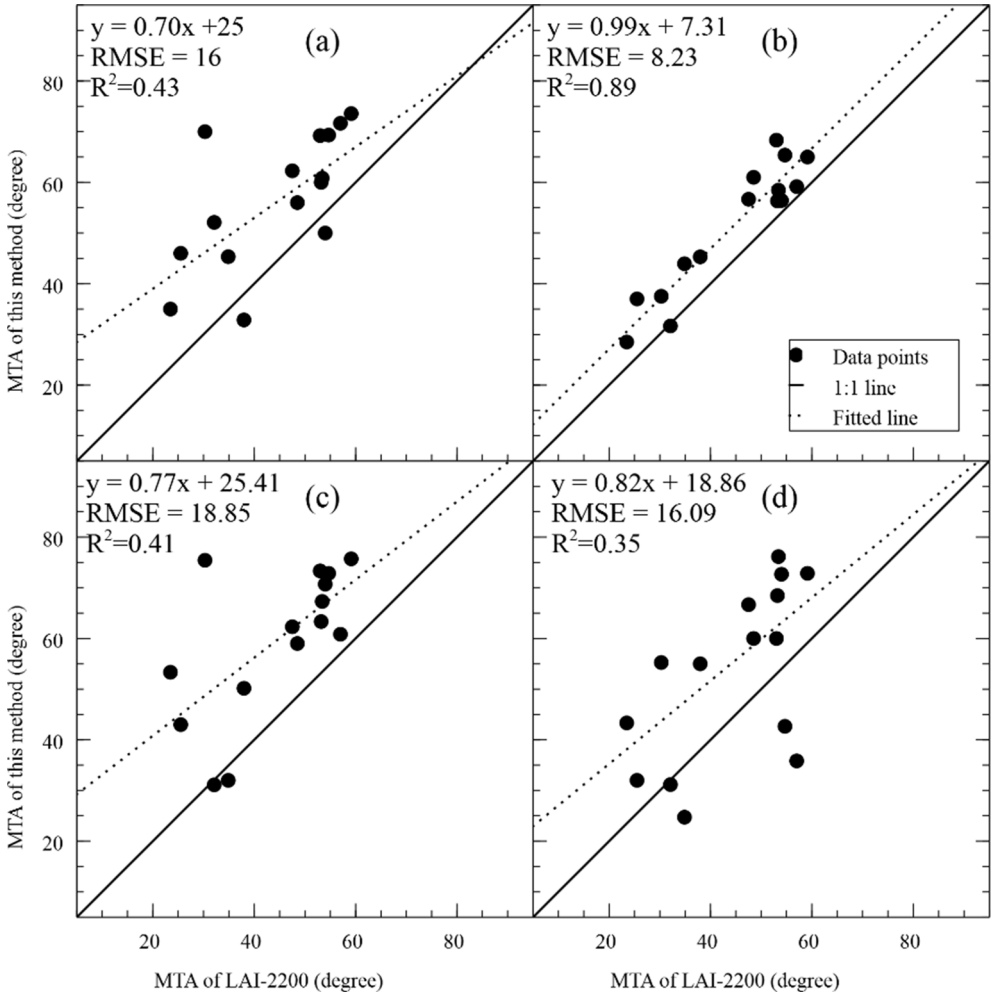

Fig. 12. Comparison of leaf mean tilt angle (MTA) estimated from the smartphone camera and measured by LAI-2200. (a)–(d) correspond to smartphone camera inclinations of 0°, 30°, 45°, and 60°, respectively.

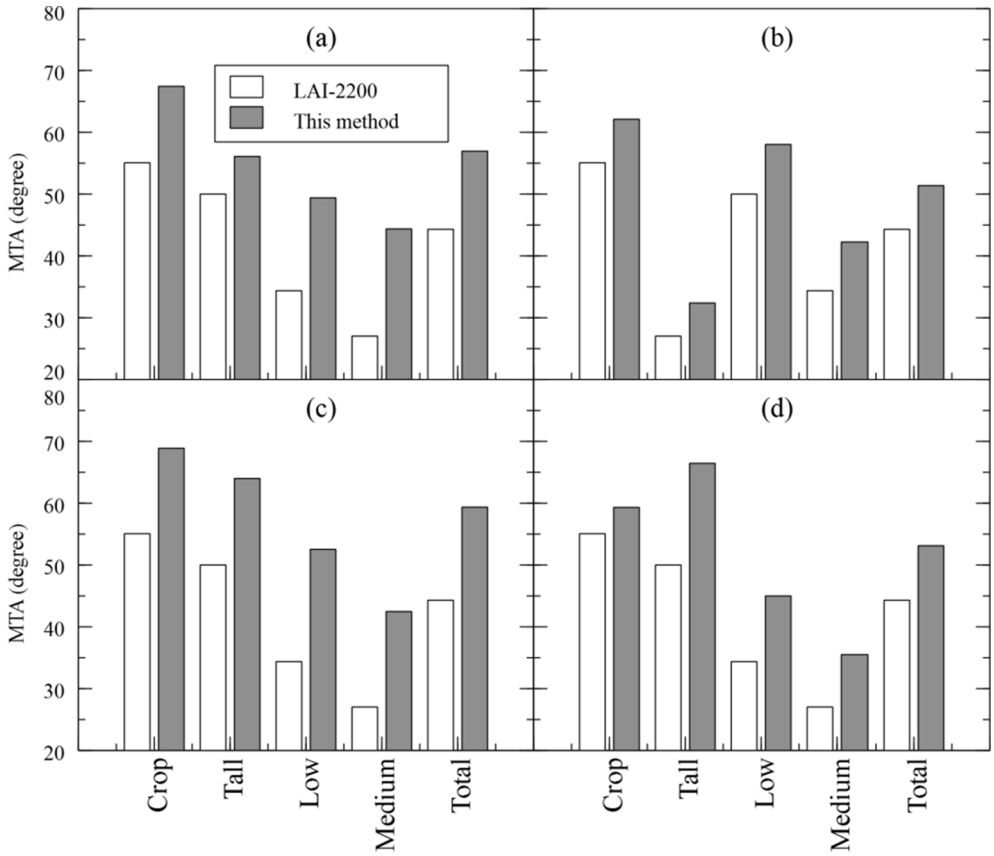

Fig. 13. Leaf mean tilt angle from LAI-2200 and inclined smartphones (this method) for different vegetation types. (a)–(d) correspond to smartphone camera inclinations of 0°, 30°, 45°, and 60°, respectively.

mode, the result has the minimum bias (RMSE = 0.59) among the four cases, and its coefficient of determination R^2 (0.68) has marginal difference with the highest value (0.71), which occurs at the mode of inclination angle 45°. The best performance of the 30° mode is also manifested by the fitted line of this method and the LAI-2200 result. The fitted line has a slope (0.96) close to one and an intercept (0.07) close to zero. As a result, the fitted line almost overlays the 1:1 line in Fig. 14b, which means that there is no significant difference between the inclination 30° mode and LAI-2200 method.

For the other 3 modes of inclination of 0°, 45° and 60°, unlike the MTA results, which share similar RMSE and R^2 values, the results for LAI have much different behaviors. For example, the RMSE ranges from 0.86 (Fig. 14c) to 1.45 (Fig. 14d), and R^2 decreases from 0.71 (Fig. 14c) to 0.39 (Fig. 14d). The ratio of the former increased by 69%, and the latter decreased by 45%. The large differences among the three modes reveal that the estimation of LAI is heavily dependent on the correct estimation of the MTA; MTA is a requirement in most camera-based LAI measurements (Meir et al., 2000). In other words, if an inappropriate MTA value is used to calculate the *G* function, the accuracy of the LAI estimate in terms of RMSE will be biased by a magnitude of up to 69%.

However, the results from two larger inclination angle modes (Fig. 14c, d) have different distributions with small inclination angle modes. The points in the two larger angle cases are distributed below the 1:1 line, especially for the case of an inclination angle of 60° (Fig. 14d), which produces the worst estimation of LAI with the highest RMSE of 1.45 and lowest R^2 of 0.39. Recalling the maximum VZA of the inclined camera in Table 2, we can partly explain the underestimation that occurs at large inclinations. When the camera is inclined from zero to a large angle, more stems or branches that are located in the lower part of the vegetation vertical profile will be observed in the smartphone camera. When the inclination angle is larger than 30°, fewer leaves will be observed with an increased inclination angle. Jointly with improper MTA as the input variable, the estimated LAI heavily departs from the reference value of LAI-2200. It should be noted that the LAI-2200 can relieve the underestimation by limiting the viewing angle below 68° (LI-COR, 2011) and isolating the effect of MTA on the LAI because they are independently estimated from the gap fraction.

The success of the 30° inclination mode can be attributed to its outperformance on MTA estimation and the inclusion of the gap fraction at lower and intermediate inclination angles from 4 to 60°. With this configuration, the VZA of the captured image has comparable range to LAI-2200, which is 7 to 68°. At this inclination angle, due to the apparent difference in the *G* functions of different MTAs, it produces the most reliable MTA from measured smartphone images. This result suggests that an inclination angle of 30° is the best solution to accurately estimate vegetation LAI and MTA using a smartphone with a narrow FOV.

When averaging the observations of multiple plots by vegetation type, it is found that the inclination of the 30° (Fig. 15b) mode works well on all types of vegetation with the lowest error. In this case, compared with the LAI-2200 measurement, the absolute errors of the estimated LAI on crop, low, medium, and tall trees are 0.37, 0.15, 0.27 and 0.28, respectively. For the other modes, the zero (Fig. 15a) mode works better on trees than crops, and the 45° (Fig. 15c) mode produces medium results. The larger inclination angle mode of 60° largely underestimates all the LAI-2200 measurements (Fig. 15d).

4.4. Prospects and limitations

Overall, the smartphone-based method shares the same principle as the normal digital camera. In the literature, either downward (Baret et al., 2010; Liu and Pattey, 2010) or upward-looking (Fuentes et al.,

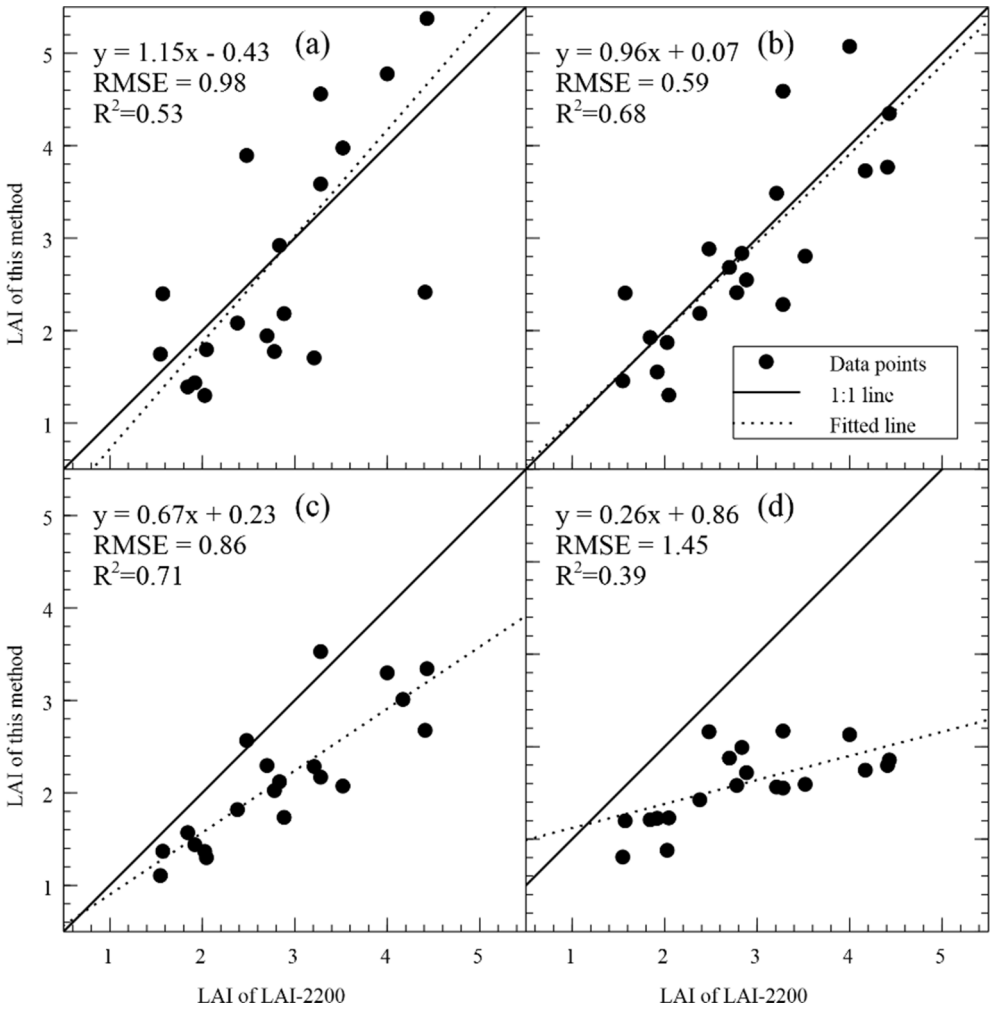

Fig. 14. Comparison of LAI estimated from a smartphone camera and measured by LAI-2200. (a)–(d) correspond to smartphone camera inclinations of 0°, 30°, 45°, and 60°, respectively.

2008; Ryu et al., 2012) modes are used to measure vegetation LAI, and the former mode is suited to short and row crops, while the latter mode has wider application ranging from crops to tall trees. The proposed method belongs to the upward-looking mode, whereas it is inclined from zenith, and by considering the convenience of multi-sensor integration (e.g., GPS, gyro and light sensor), the portability (light weight and small size) and the computing capability (real-time reporting result on site), the smartphone-based method is much more attractive than the normal digital camera.

Accurate estimation of leaf MTA and the use of MTA to improve the performance of LAI measurements on site are valuable contributions of our method. To our knowledge, our work is the first to simultaneously measure the leaf MTA and LAI from smartphone camera images. Although LAI has been a hot topic in vegetation structural measurement using smartphones (Aquino et al., 2015; Bauer et al., 2016; Confalonieri et al., 2013; De Bei et al., 2016; Fuentes et al., 2012; Qu et al., 2017), the measurement of leaf MTA using smartphones has not yet been reported widely. In addition, although MTA can be measured using digital photography with regular cameras (Zou et al., 2014), the estimation of leaf angle is time consuming because image processing is conducted indoors with a computer. Confalonieri et al. (2017) proposed a smartphone APP - PocketPlant3D to analyze canopy structure, including leaf angle. The app measures the leaf angle by handholding the smartphone parallel to the leaf lamina while moving slowly and recording the output of the device accelerometer and magnetometer to calculate the leaf angle. From the operation illustration of the app, the method is limited to plants with short broadleaf crops, e.g., maize. Unlike PocketPlant3D, we use images captured by a series of shoots while moving under (for trees) or within (for crop) canopies; as a result, our proposed method offers higher operational efficiency and broader applications.

Although ground truth data collected by destructive methods are ideal to validate a novel method, limited by actual field work conditions to respect the restriction of farmer management, no destructive LAI was collected, and the validation data came from the measurements of LAI-2200. Currently, we have not evaluated the uncertainty of the LAI-2200 measurement in this study. Analysis of MTA and LAI from the LAI-2200 (or its predecessor LAI-2000) instrument can be found in the literature, for example, Zou et al. (2014) on MTA and Liu et al (2015) on LAI.

We read the inclination angle from a smartphone screen and captured an image by touching the screen, so reading and touching actions are needed for every image. In future work, an automatic trigger as implemented by PocketLAI (Confalonieri et al., 2014) might be desired to accelerate the speed of capturing images. Specifically, when the smartphone is inclined to the user-defined angle (e.g., 30° in this work), the app will detect the smartphone posture and capture one image automatically. We believe this new function will improve the efficiency of field work.

As a photographic approach, the proposed method will also be affected by segment accuracy which classifies pixels into sky and leaves. Post-processing algorithm that can reduce large gaps caused by over-exposure might improve the performance of estimated LAI (Fang et al., 2018). However, complicated algorithm needs running on

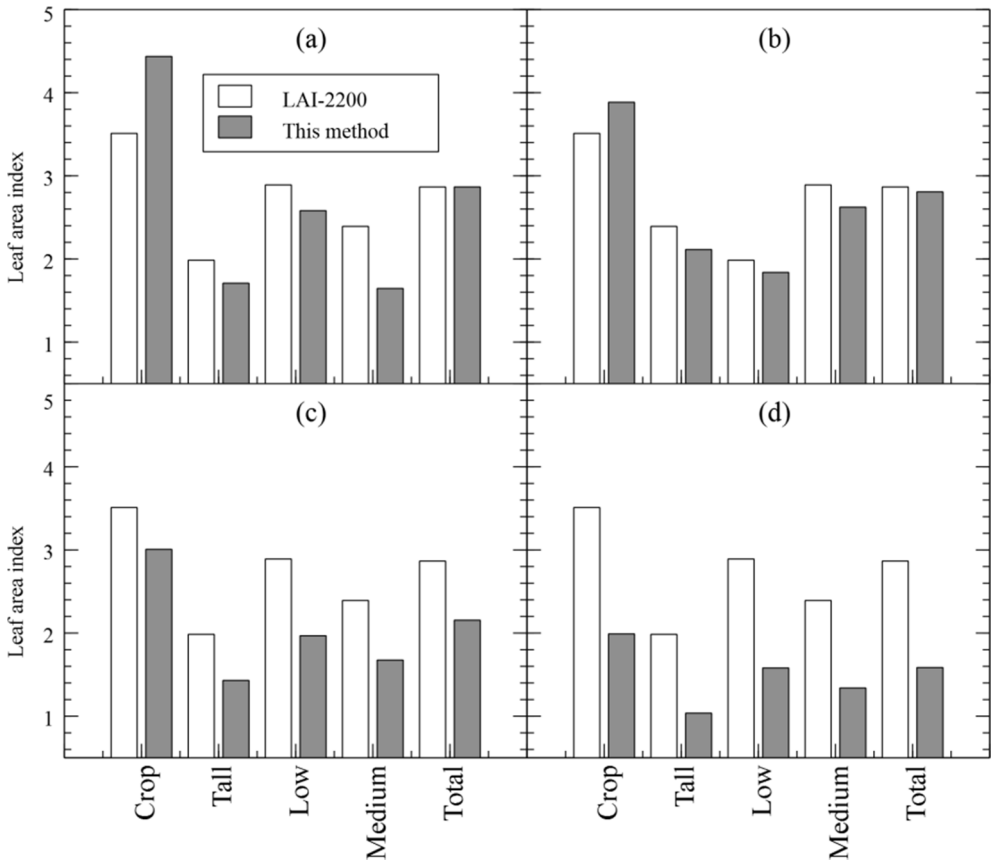

Fig. 15. Leaf area index of LAI-2200 and inclined camera (this method) for different vegetation types. (a)–(d) correspond to smartphone camera inclinations of 0°, 30°, 45°, and 60°, respectively.

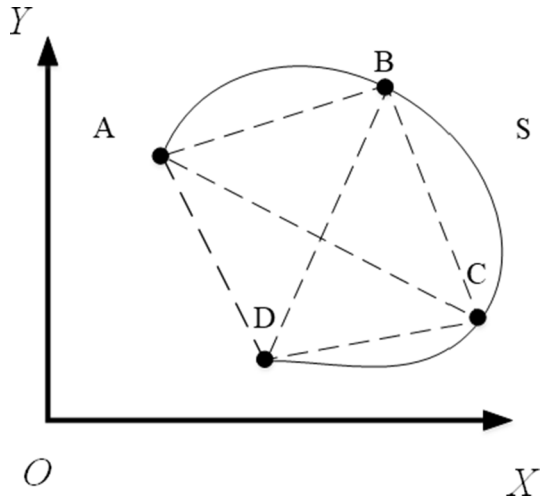

Fig. A1. Curves and corners.

computer, and considering the calculation resource consumed by smartphone, we used the simple automation threshold (Otsu, 1979). This method has a wide application in image processing, and has proven to perform well for images with enough intensity difference (Goh et al., 2018), which can be easily achieved by taking images under diffused light condition.

Finally, other factors related to the proposed method are computation efficiency and error of the result when images are acquired with a smartphone. From the statistical perspective, more images in one plot means more samples to the whole distribution of canopy structure, and smaller bin of zenith angle in one image means more gap fraction to calculate *G* function. The effort on increasing count of images in one plot or zenith angles in one image might help to improve the accuracy of LAI and MTA. However, the cost is to increase field work intensity and more computation time of smartphone CPU. An analysis on the optimized number of images in one plot and the number of bins of zenith angles in one image is presented in Appendix B.

5. Conclusion

The effectiveness of using an inclined smartphone camera for measuring leaf area index (LAI) was investigated in this study. To overcome the limitation of the narrow field of viewing (FOV) of common consumer-grade smartphone cameras, we proposed a method to enlarge the effective viewing zenith angle (VZA). In our method, the smartphone was inclined to capture a series of images in a plot, and the images in this mode were analyzed to calculate directional gap fractions, which were then used to derive the canopy *G* function and mean tilt angle (MTA). The results confirm that the smartphone-based technique, as an alternative to classical commercial instruments, can accurately measure the LAI when it was inclined in the degree near the camera's maximum half FOV angle. The best performance of LAI was observed at an inclination of 30° when a camera with a FOV of 70° was used. The improvement of the performance of LAI was attributed to the accurate calculation of the MTA at this inclination angle with the help of an enlarged effective VZA. The errors of estimated LAI are related to the number of images used to obtain the averaged LAI in a plot and the size of the VZA bin that is used to generate the directional gap fractions. The results suggest that approximately 7–9 images in one plot and a binning size of 5° for the VZA ring would produce acceptable results when both efficiency and performance are considered (see Appendix B). Although MTA was

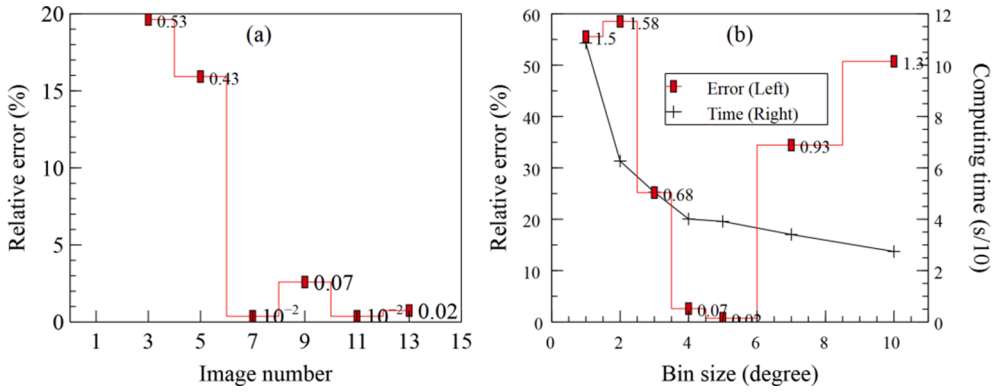

Fig. B1. Factors related to the performance of the estimated LAI. (a) Relative errors (red line) and absolute errors (red points) varying with the image number. (b) Relative and absolute errors (red line and points of left axis) and the computing time (black line of the right axis is scaled by 10) varying with the size of the zenith angle bin.

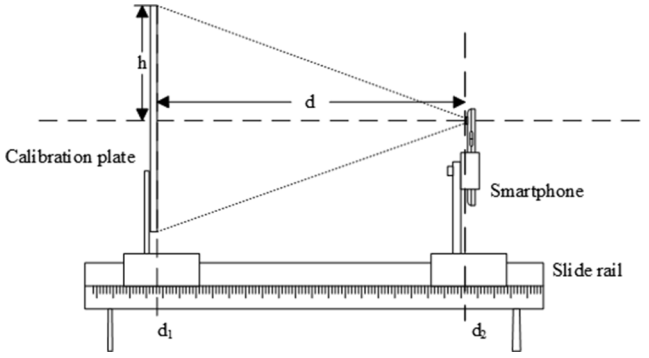

Fig. C1. Experiment setup of measurement on camera FOV of smartphone. The distance (d) between calibration plate (d_1) and smartphone (d_2) can be adjusted by moving slide rail.

Table C1
Data collected in the experiment.

	h (cm)	d (cm)	tanθ	θ (°)	FOV (°)
1	18.187	24.94	0.729	36.10	72.20
2	18.187	25.50	0.713	35.50	71.00
3	18.187	25.78	0.705	35.20	70.40

derived as an intermediate result of the target variable of LAI, the results showed a potential for simultaneous measurement of vegetation MTA and LAI for the scenario in which the two canopy structural parameters are desired.

The smartphone app (LAISmart) used in this work is available from Huawei App Gallery (Chinese version) or GitHub (English version, https://github.com/niugankeji/diyaobao_English).

Declaration of Competing Interest

The authors declare that they have no known competing financial interests or personal relationships that could have appeared to influence the work reported in this paper.

Acknowledgements

This work was supported in part by the National Natural Science Foundation of China (41671333). Datasets from ZY region were collected with the help of graduate students Luo Tian, Dantong Wang, and Chuqiao Hong. We thank the above students for their hard filed work. We acknowledge researchers Tao Che and Rui Jin from Heihe Remote Sensing Experimental Research Station in Northwest Institute of Eco-environment and Resources CAS, Professor Mingguo Ma from Chongqing Jinfo Mountain Karst Ecosystem National Observation and Research Station, for providing support to the field experiment. All the figures were plotted by software Veusz (https://veusz.github.io) and QGIS (https://www.qgis.org). We are grateful to the contributors of the open source software.

Appendix A. Curve matching of normalized corner distance matrix (NCDM) algorithm and its source code in JAVA language

1. Algorithm

In this paper, the shape matching algorithm named normalized corner distance matrix (NCDM) is used to match the G function and the average contact number C(θ). The principle of curve matching is to describe the shape of a curve using a series of points. In this process, the points on the curve are sampled uniformly and N corners are selected, as shown in Fig. A1. it is assumed that the vector on these corners can express the shape and trend of the curve. As an example, in Fig. A1, the corners A, B, C, and D on curve S and their coordinates are used to describe the shape of the curve. In this context, more corners mean more accurate description on the shape. However, we cannot infinitely increase the corners limited by the computing efficiency, so in this study, only points lying on the viewing zenith angles are selected to match both curves.

For any curve, let's say it has several corners c_1, c_2, c_3 … c_n, and the corresponding coordinates are $(x_1 y_1)$, $(x_2 y_2)$, $(x_3 y_3)$…$(x_n y_n)$. The distance between the corners can determine the mutual position between the corners, and the matrix composed by the distance between the corners is called the corner distance matrix (CDM).

Here, we present detailed description on CDM. The corner distance matrix is an $N \times N$ square matrix established by the Euclidean distance between corners, and its row is the Euclidean distance between a corner point and all other corners,

$$\mathrm{D}=\begin{Bmatrix} d_{1,1} & d_{1,2} & \cdots & d_{1,\mathrm{n}} \\ d_{2,1} & d_{2,2} & \cdots & d_{2,\mathrm{n}} \\ \cdots & \cdots & \cdots & \cdots \\ d_{\mathrm{n},1} & d_{\mathrm{n},\mathrm{n}} & \cdots & d_{\mathrm{n},\mathrm{n}} \end{Bmatrix} \tag{A1}$$

where

$$d_{i,j}=\sqrt{\left(x_i-x_j\right)^2+\left(y_i-y_j\right)^2} \tag{A2}$$

The CDM can be normalized by the maximum distance from elements in Eq. (A1), So the normalized matrix reflects the contour information of the curve. It is invariant to the translation, rotation, and scaling conducted on the original curve. As a result, the original distance matrix now is rewritten as

$$\mathrm{D}=\begin{Bmatrix} \frac{d_{1,1}}{d_{max}} & \frac{d_{1,2}}{d_{max}} & \cdots & \frac{d_{1,n}}{d_{max}} \\ \frac{d_{2,1}}{d_{max}} & \frac{d_{2,2}}{d_{max}} & \cdots & \frac{d_{2,n}}{d_{max}} \\ \cdots & \cdots & \cdots & \cdots \\ \frac{d_{n,1}}{d_{max}} & \frac{d_{n,2}}{d_{max}} & \cdots & \frac{d_{n,n}}{d_{max}} \end{Bmatrix}=\begin{Bmatrix} \phi_{1,1} & \phi_{1,2} & \cdots & \phi_{1,n} \\ \phi_{1,2} & \phi_{2,2} & \cdots & \phi_{2,n} \\ \cdots & \cdots & \cdots & \cdots \\ \phi_{1,n} & \phi_{2,n} & \cdots & \phi_{n,n} \end{Bmatrix} \tag{A3}$$

$$\text{where } d_{max}=\max\left(d_{i,j}\right) \tag{A4}$$

And the matrix in Eq. (A3) is called normalized corner distance matrix (NCDM).

In the process of shape matching between $\mathrm{G}(\theta)$ and $\mathrm{C}(\theta)$, the trend or direction of the curve must be considered. It can be easily understood that only those curves having same directions can be regarded as the similar curve. So the NCDM is modified as the following equation to reflect the curve direction, and it is denoted as the improved normalized corner distance matrix (INCDM).

$$\mathrm{D}=\begin{Bmatrix} \frac{d_{1,1}}{d_{max}} & \frac{d_{1,2}}{d_{max}} & \cdots & \frac{d_{1,n}}{d_{max}} \\ \frac{d_{2,1}}{d_{max}} & \frac{d_{2,2}}{d_{max}} & \cdots & \frac{d_{2,n}}{d_{max}} \\ \cdots & \cdots & \cdots & \cdots \\ \frac{d_{n,1}}{d_{max}} & \frac{d_{n,2}}{d_{max}} & \cdots & \frac{d_{n,n}}{d_{max}} \end{Bmatrix}=\begin{Bmatrix} \phi_{1,1} & \phi_{1,2} & \cdots & \phi_{1,n} \\ \phi_{1,2} & \phi_{2,2} & \cdots & \phi_{2,n} \\ \cdots & \cdots & \cdots & \cdots \\ \phi_{1,n} & \phi_{2,n} & \cdots & \phi_{n,n} \end{Bmatrix} \tag{A5}$$

$$d_{i,j}=\begin{cases} \sqrt{\left(x_i-x_j\right)^2+\left(y_i-y_j\right)^2} & \frac{x_i-x_j}{y_i-y_j}\geq 0 \\ -\sqrt{\left(x_i-x_j\right)^2+\left(y_i-y_j\right)^2} & \frac{x_i-x_j}{y_i-y_j}<0 \end{cases} \tag{A6}$$

$$d_{max}=\max\left(\left|d_{i,j}\right|\right) \tag{A7}$$

The difference between INCDM and NCDM is that the calculation on the distance between two points. In the original matrix, NCDM, distance is calculated using the normal Euclidean distance and all the distance is positive values, whereas in the improved matrix, INCDM, the distance can be negative value in the case its slope is negative.

For any two curves, e.g., A and B, the ratio of the elements in their INCDM can be used to denote the discrimination of A and B,

$$\Phi_{A,B}=\begin{Bmatrix} \frac{\phi^A_{1,1}}{\phi^B_{1,1}} & \frac{\phi^A_{1,2}}{\phi^B_{1,2}} & \cdots & \frac{\phi^A_{1,n}}{\phi^B_{1,n}} \\ \frac{\phi^A_{2,1}}{\phi^B_{2,1}} & \frac{\phi^A_{2,2}}{\phi^B_{2,2}} & \cdots & \frac{\phi^A_{2,n}}{\phi^B_{2,n}} \\ \cdots & \cdots & \cdots & \cdots \\ \frac{\phi^A_{n,1}}{\phi^B_{n,1}} & \frac{\phi^A_{2,n}}{\phi^B_{2,n}} & \cdots & \frac{\phi^A_{n,n}}{\phi^B_{n,n}} \end{Bmatrix} \tag{A8}$$

In the above discrimination matrix, the value of the elements can reflect the difference between two segments.

By considering the direction of curve, we calculate the direction coefficient U as

$$\mathrm{U}=\sum_{i=1}^{n}\sum_{j=1}^{n}\Phi_{i,j} \tag{A9}$$

Then the coefficient of discriminability (COD) between curves A and B can be calculated as

$$w = \begin{cases} \sum_{i=1}^{n}\sum_{j=1}^{n}|\Phi_{i,j}|U \geq 0 \\ -\sum_{i=1}^{n}\sum_{j=1}^{n}|\Phi_{i,j}|U < 0 \end{cases} \tag{A10}$$

The COD calculated as W in Eq.(A10) can be used as the discrimination index of the two curves. When W greater than 0, it means that the two curves have the same trend and larger magnitude of COD means larger difference between curves. When $w < 0$, it means that the two curves have totally opposite trends and in this case, they are definitely two different curves.

While the above procedure is used to compare any $C(\theta)$ with simulated $G(\theta)$, we select the $G(\theta)$ as the optimization from all the candidates for the one that has smallest COD value.

2. Java code

```
/**
     * Calculate Normalized corner distance matrix
     *
     * @param × vertical coordinates
     * @param y vertical coordinates
     * (x, y) is the coordinate of the corner of the curve.
     * @return Normalized corner distance matrix
     *
   public static double[][] distance_matrix(double[] ×, double[] y) {
     int n = x.length; // dimension
     double max = 0; //max value of corner distance
     double[][] distance = new double[n][n]; // Normalized corner distance matrix
     for (int i = 0; i < n; i++) {
       for (int j = 0; j < n; j++) {
         if((x[j] - x[i])*(j - i) >= 0){
           distance[i][j] = Math.sqrt(Math.pow(x[i]-x[j],2) + Math.pow(y[i] – y[j]),2);
         }
         else{
           distance[i][j] = - Math.sqrt((x[i]-x[j]) * (x[i] - x[j]) + (i - j) * (i - j));
         }
         if (max <= Math.abs(distance[i][j])) {
           max = Math.abs(distance[i][j]); //find max corner distance
         }
if(distance[i][j] == 0){
           distance[i][j] = 0.0001; // Make sure the dividend is not zero
         }
       }
     }
     for (int i = 0; i < n; i++) {
       for (int j = 0; j < n; j++) {
         distance[i][j] = distance[i][j] / max; // Normalized
       }
     }
     return distance;
}
/**
     * @param a1 first Normalized corner distance matrix
     * @param a2 second Normalized corner distance matrix
     * @return The difference coefficient W
     */
   private static double similar_judge(double[][] a1, double[][] a2) {
     int cols = a1.length; // dimension
     double w = 0; // The difference coefficient W
     double[][] sim = new double[cols][cols]; //similar matrix
     double U = 0; // direction coefficient U
     for (int i = 0; i < cols; i++) {
       for (int j = 0; j < cols; j++) {
         sim[i][j] = a1[i][j] / a2[i][j];
         U = U + sim[i][j];
         sim[i][j] = Math.abs(sim[i][j]);
         w = w + Math.abs((1 - sim[i][j]));
       }
     }
     if(mean < 0){
       w = - w;
     }
     return w;
   }
```

Appendix B. Potential error source and computing efficiency of inclined smartphone method

In the analysis of the error source, we investigate two sources that might affect the LAI result, i.e., the image number in one plot used to estimate the averaged LAI in plot scale and the size of the zenith angle bin, which is used to group image pixels into different VZA rings, and regarding the latter factor, the computing time on one image is also recorded to analyze the efficiency of the algorithm.

As indicated in Fig. B1(a), with the increased image number in one plot, the errors decrease dramatically. The maximum errors (RE of 20% and AE of 0.53) are observed when only three images are used, whereas an RE of 1% and AE of 0.01 to 0.07 occur in the case of 7 or more images. This result means that more sampling data from field work are capable of representing the spatial distribution of vegetation LAI in one plot. However, more images mean more time spent on labor in the field and thus low work efficiency per plot. Considering the LAI requirements of applications, e.g., AE $<$ 0.5 and RE $<$ 20% (GCOS, 2011), the number of images required to produce acceptable results will be approximately 7–9.

Another factor, the size of the zenith angle bin, will affect the resolution of VZA rings while grouping all the pixels into different VZA rings in one image. For an image captured by a camera of fixed FOV, a larger bin angle means more pixels in one bin and thus a lower number of VZAs. As a result, a larger bin size may improve the computing efficiency with a lower number of VZAs; however, it will sacrifice the resolution of the VZA ring and may affect the performance of the matched G function when directional gap fractions on different VZAs are used. In this work, the bin size is determined such that it is small enough to ensure that there are sufficient angles of the gap fraction to match the theoretical G function and that it is large enough to ensure that there are sufficient pixels to calculate the gap fraction at that angle. Therefore, the bin size is related not only to the LAI accuracy but also to the computing efficiency. In general, the computing time decreases from 1.2 s to 0.25 s per image as the size of the zenith angle bin increases from 1° to 10° (Fig. B1(b)). However, the errors of the estimated LAI do not show a monotonic decrease with increasing bin size. When the bin size is in the range from 3° to 6°, the errors decrease to the minimum. In addition, after that point, an increasing trend is observed. This is because when the bin size is larger than 6°, only fewer zenith bins ($<$5) can be recognized, and it is more difficult to match the optimized G function with such fewer directional gap fractions. As a result, the final selection of bin size may be the compromise of computing efficiency and requirement of accuracy.

We chose a VZA bin size of 5°, and this configuration produces a number of directional gap fractions ranging from 7 to 11 for most consumer-grade smartphones. The results show that a resolution of 5° is reasonable for the configuration of the smartphone we used. However, with the new release of higher configurations on smartphones, for example, the ultra-wide FOV camera in the Huawei P40 series is 100° (Huawei, 2020) and that in the IPhone12 series is 120° (Apple, 2020), the bin size will be changed accordingly.

Appendix C. Experiment on calculating field of viewing (FOV) angle of smartphone camera

To verify the full field of viewing (FOV) angle is in a narrow range, i.e., about 70° in this paper, we designed an experiment to calculate FOV of the smartphone

In this experiment, a smartphone (Huawei Honor 7 Model) and a calibration plate (a white A4 size paper) were placed at two ends of slide rail which functions to adjust the distance between smartphone and calibration plate as illustrated in Fig. C1.

When experiment started, we took photo of calibration at different distance. Once the calibration plate was fully shown in the field of camera previous screen, then the camera was triggered, and in the meantime, we recorded the readings of d_1 and d_2. Then the distance between smartphone and calibration plate was calculated as

$$d = |d_1 - d_2|. \tag{C1}$$

Three replications were conducted on the above procedure, and the data were listed in Table C1.

The half FOV (θ) was calculated as

$$\tan\theta = \frac{h}{d} \tag{C2}$$

It should be noted that, in this experiment, the distance was slightly differenced in the three replications and the height was fixed. This height is the full height of calibration plate.

From the result of experiment, the FOV was in the range of 70.40° to 72.20°, and for simplify calculation, the final FOV was set as 70°.

References

Anonymous, 2015. Peer review report 2 On "Photographic measurement of leaf angles in field crops". Agric. For. Meteorol. 201, 318. https://doi.org/10.1016/j.agrformet.2015.08.103.

Apple, 2020. iPhone 12 Pro and 12 Pro Max - Technical Specifications - Apple [WWW Document]. Apple. URL https://www.apple.com/iphone-12-pro/specs/ (accessed 2.2.21).

Aquino, A., Millan, B., Gaston, D., Diago, M.-P., Tardaguila, J., 2015. vitisFlower®: Development and Testing of a Novel Android-Smartphone Application for Assessing the Number of Grapevine Flowers per Inflorescence Using Artificial Vision Techniques. Sensors 15 (9), 21204–21218.

Baret, F., de Solan, B., Lopez-Lozano, R., Ma, K., Weiss, M., 2010. GAI estimates of row crops from downward looking digital photos taken perpendicular to rows at 57.5° zenith angle: Theoretical considerations based on 3D architecture models and application to wheat crops. Agric. For. Meteorol. 150 (11), 1393–1401. https://doi.org/10.1016/j.agrformet.2010.04.011.

Bauer, J., Siegmann, B., Jarmer, T., Aschenbruck, N., 2016. Smart fLAIr: A smartphone application for fast LAI retrieval using Ambient Light Sensors. In: SAS 2016 - Sensors Applications Symposium, Proceedings. Institute of Electrical and Electronics Engineers Inc, pp. 401–406. https://doi.org/10.1109/SAS.2016.7479880.

Bréda, N.J.J., 2003. Ground-based measurements of leaf area index: a review of methods, instruments and current controversies. J. Exp. Bot. 54, 2403–2417. https://doi.org/10.1093/jxb/erg263.

Campbell, G.S., 1990. Derivation of an angle density function for canopies with ellipsoidal leaf angle distributions. Agric. For. Meteorol. 49, 173–176. https://doi.org/10.1016/0168-1923(90)90030-A.

Campbell, G.S., 1986. Extinction coefficients for radiation in plant canopies calculated using an ellipsoidal inclination angle distribution. Agric. For. Meteorol. 36 (4), 317–321.

Chen, J.M., Black, T.A., 1992. Defining leaf area index for non-flat leaves. Plant. Cell Environ. 15 (4), 421–429. https://doi.org/10.1111/j.1365-3040.1992.tb00992.x.

Chen, J.M., Cihlar, J., 1995. Plant canopy gap-size analysis theory for improving optical measurements of leaf-area index. Appl. Opt. 34 (27), 6211. https://doi.org/10.1364/AO.34.006211.

Chen, J.M., Rich, P.M., Gower, S.T., Norman, J.M., Plummer, S., 1997. Leaf area index of boreal forests: Theory, techniques, and measurements. J. Geophys. Res. 102 (D24), 29429–29443.

Chianucci, F., Cutini, A., 2013. Estimation of canopy properties in deciduous forests with digital hemispherical and cover photography. Agric. For. Meteorol. 168, 130–139. https://doi.org/10.1016/j.agrformet.2012.09.002.

Confalonieri, R., Foi, M., Casa, R., Aquaro, S., Tona, E., Peterle, M., Boldini, A., De Carli, G., Ferrari, A., Finotto, G., Guarneri, T., Manzoni, V., Movedi, E., Nisoli, A., Paleari, L., Radici, I., Suardi, M., Veronesi, D., Bregaglio, S., Cappelli, G., Chiodini, M.E., Dominoni, P., Francone, C., Frasso, N., Stella, T., Acutis, M., 2013. Development of an app for estimating leaf area index using a smartphone. Trueness and precision determination and comparison with other indirect methods. Comput. Electron. Agric. 96, 67–74. https://doi.org/10.1016/j.compag.2013.04.019.

Confalonieri, R., Francone, C., Foi, M., 2014. The PocketLAI smartphone app: An alternative method for leaf area index estimation. In: Proceedings - 7th International Congress on Environmental Modelling and Software: Bold Visions for Environmental Modeling, IEMSs 2014. iEMSs, San Diego, CA, USA, pp. 288–293.

Confalonieri, R., Paleari, L., Foi, M., Movedi, E., Vesely, F.M., Thoelke, W., Agape, C., Borlini, G., Ferri, I., Massara, F., Motta, R., Ravasi, R.A., Tartarini, S., Zoppolato, C., Baia, L.M., Brumana, A., Colombo, D., Curatolo, A., Fauda, V., Gaia, D., Gerosa, A., Ghilardi, A., Grassi, E., Magarini, A., Novelli, F., Perez Garcia, F.B., Rota Graziosi, A., Salvan, M., Tadiello, T., Rossini, L., 2017. PocketPlant3D: Analysing canopy structure using a smartphone. Biosyst. Eng. 164, 1–12. https://doi.org/10.1016/j.biosystemseng.2017.09.014.

De Bei, R., Fuentes, S., Gilliham, M., Tyerman, S., Edwards, E., Bianchini, N., Smith, J., Collins, C., 2016. VitiCanopy: A Free Computer App to Estimate Canopy Vigor and Porosity for Grapevine. Sensors 16, 585. https://doi.org/10.3390/s16040585.

Fang, H., Ye, Y., Liu, W., Wei, S., Ma, L., 2018. Continuous estimation of canopy leaf area index (LAI) and clumping index over broadleaf crop fields: An investigation of the PASTIS-57 instrument and smartphone applications. Agric. For. Meteorol. 253–254, 48–61. https://doi.org/10.1016/j.agrformet.2018.02.003.

Fuentes, S., Bei, R.D., Pozo, C., Tyerman, S., 2012. Development of a smartphone application to characterise temporal and spatial canopy architecture and leaf area index for grapevines. Wine Vitic. J. 27, 56–60.

Fuentes, S., Palmer, A.R., Taylor, D., Zeppel, M., Whitley, R., Eamus, D., 2008. An automated procedure for estimating the leaf area index (LAI) of woodland ecosystems using digital imagery, MATLAB programming and its application to an examination of the relationship between remotely sensed and field measurements of LAI. Funct. Plant Biol. 35 (10), 1070. https://doi.org/10.1071/FP08045.

G.Lang, A.R., 1987. Simplified estimate of leaf area index from transmittance of the sun's beam. Agric. For. Meteorol. 41, 179–186. https://doi.org/10.1016/0168-1923(87)90078-5.

GCOS, 2011. Systematic observation requirements for satellite-based data products for climate. Supplemental Details to the Satellite-based Component of the Implementation Plan for the Global Observing System for Climate in Support of the UNFCCC (2010 Update).

Goh, T.Y., Basah, S.N., Yazid, H., Juhairi, M., Safar, A., 2018. Performance analysis of image thresholding: Otsu technique. Measurement 114, 298–307. https://doi.org/10.1016/j.measurement.2017.09.052.

Gonsamo, A., Walter, J.-M., Chen, J.M., Pellikka, P., Schleppi, P., 2018. A robust leaf area index algorithm accounting for the expected errors in gap fraction observations. Agric. For. Meteorol. 248, 197–204. https://doi.org/10.1016/j.agrformet.2017.09.024.

Huawei, 2020. HUAWEI P40 Pro+ Specifications [WWW Document]. Huawei. URL https://consumer.huawei.com/en/phones/p40-pro-plus/specs (accessed 2.2.21).

ImageJ, 2020. ImageJ [WWW Document]. ImageJ. URL https://imagej.nih.gov/ij/ (accessed 2.2.21).

Jonckheere, I., Fleck, S., Nackaerts, K., Muys, B., Coppin, P., Weiss, M., Baret, F., 2004. Review of methods for in situ leaf area index determination: Part I. Theories, sensors and hemispherical photography. Agric. For. Meteorol. 121 (1-2), 19–35.

Knisley, J., 2001. Multivariable Calculus [WWW Document]. East Tennessee State Univ. URL https://math.etsu.edu/multicalc/prealpha/Chap3/Chap3-1/index.htm (accessed 6.23.21).

LI-COR, 2011. LAI-2200 Plant Canopy Analyser Instruction Manual.

Liu, C., Kang, S., Li, F., Li, S., Du, T., 2013. Canopy leaf area index for apple tree using hemispherical photography in arid region. Sci. Hortic. (Amsterdam) 164, 610–615. https://doi.org/10.1016/j.scienta.2013.10.009.

Liu, J., Pattey, E., 2010. Retrieval of leaf area index from top-of-canopy digital photography over agricultural crops. Agric. For. Meteorol. 150 (11), 1485–1490. https://doi.org/10.1016/j.agrformet.2010.08.002.

Liu, Z., Jin, G., Zhou, M., 2015. Evaluation and correction of optically derived leaf area index in different temperate forests. iForest –. Biogeosci. For. 9 (1), 55–62.

Meir, P., Grace, J., Miranda, A.C., 2000. Photographic method to measure the vertical distribution of leaf area density in forests. Agric. For. Meteorol. 102 (2-3), 105–111. https://doi.org/10.1016/S0168-1923(00)00122-2.

Miller, J.B., 1967. A formula for average foliage density. Aust. J. Bot. 15, 141–144. https://doi.org/10.1071/BT9670141.

Nilson, T., 1971. A theoretical analysis of the frequency of gaps in plant stands. Agric. Meteorol. 8, 25–38. https://doi.org/10.1016/0002-1571(71)90092-6.

Otsu, N., 1979. A Threshold Selection Method from Gray-Level Histograms. IEEE Trans. Syst. Man Cybern. 9 (1), 62–66. https://doi.org/10.1109/TSMC.1979.4310076.

Pisek, J., Ryu, Y., Alikas, K., 2011. Estimating leaf inclination and G-function from leveled digital camera photography in broadleaf canopies. Trees - Struct. Funct. 25 (5), 919–924. https://doi.org/10.1007/s00468-011-0566-6.

Pisek, J., Sonnentag, O., Richardson, A.D., Mõttus, M., 2013. Is the spherical leaf inclination angle distribution a valid assumption for temperate and boreal broadleaf tree species? Agric. For. Meteorol. 169, 186–194. https://doi.org/10.1016/j.agrformet.2012.10.011.

Qi, J., Xie, D., Li, L., Zhang, W., Mu, X., Yan, G., 2019. Estimating Leaf Angle Distribution from Smartphone Photographs. IEEE Geosci. Remote Sens. Lett. 16 (8), 1190–1194. https://doi.org/10.1109/LGRS.885910.1109/LGRS.2019.2895321.

Qu, Y., Meng, J., Wan, H., Li, Y., 2016. Preliminary study on integrated wireless smart terminals for leaf area index measurement. Comput. Electron. Agric. 129, 56–65. https://doi.org/10.1016/j.compag.2016.09.011.

Qu, Y., Shaker, A., Korhonen, L., Silva, C.A., Jia, K., Tian, L., Song, J., 2020. Direct Estimation of Forest Leaf Area Index based on Spectrally Corrected Airborne LiDAR Pulse Penetration Ratio. Remote Sens. 12 (2), 217. https://doi.org/10.3390/rs12020217.

Qu, Y., Wang, J., Song, J., Wang, J., 2017. Potential and Limits of Retrieving Conifer Leaf Area Index Using Smartphone-Based Method. Forests 8 (6), 217. https://doi.org/10.3390/f8060217.

Raabe, K., Pisek, J., Sonnentag, O., Annuk, K., 2015. Variations of leaf inclination angle distribution with height over the growing season and light exposure for eight broadleaf tree species. Agric. For. Meteorol. 214–215, 2–11. https://doi.org/10.1016/j.agrformet.2015.07.008.

Rao, R., 2021. Computer Vision Course [WWW Document]. URL https://courses.cs.washington.edu/courses/cse455/ (accessed 7.24.21).

Ross, J., 1981. The Radiation Regime and Architecture of Plant Stands. The Hague, W. Junk.

Ryu, Y., Nilson, T., Kobayashi, H., Sonnentag, O., Law, B.E., Baldocchi, D.D., 2010a. On the correct estimation of effective leaf area index: Does it reveal information on clumping effects? Agric. For. Meteorol. 150 (3), 463–472. https://doi.org/10.1016/j.agrformet.2010.01.009.

Ryu, Y., Sonnentag, O., Nilson, T., Vargas, R., Kobayashi, H., Wenk, R., Baldocchi, D.D., 2010b. How to quantify tree leaf area index in an open savanna ecosystem: A multi-instrument and multi-model approach. Agric. For. Meteorol. 150, 63–76. https://doi.org/10.1016/j.agrformet.2009.08.007.

Ryu, Y., Verfaillie, J., Macfarlane, C., Kobayashi, H., Sonnentag, O., Vargas, R., Ma, S., Baldocchi, D.D., 2012. Continuous observation of tree leaf area index at ecosystem scale using upward-pointing digital cameras. Remote Sens. Environ. 126, 116–125. https://doi.org/10.1016/j.rse.2012.08.027.

Vicent Agustí Ribas Costa, 2021. Design and validation of a new technique for estimating canopy parameters: UAS-based spherical(360)photography, description of the forest canopy from inside. University of Helsinki.

Weiss, M., Baret, F., 2017. Can_Eye V6.4.91 User Manual [WWW Document]. URL https://www6.paca.inra.fr/can-eye/News/CAN-EYE-V6.49-Release (accessed 3.20.20).

Weiss, M., Baret, F., Smith, G.J., Jonckheere, I., Coppin, P., 2004. Review of methods for in situ leaf area index (LAI) determination: Part II. Estimation of LAI, errors and sampling. Agric. For. Meteorol. 121 (1-2), 37–53.

Welles, J.M., 1990. Some indirect methods of estimating canopy structure. Remote Sens. Rev. 5 (1), 31–43. https://doi.org/10.1080/02757259009532120.

Wilson, JW, 1963. Estimation of foliage denseness and foliage angle by inclined point quadrats. Aust. J. Bot. 11 (1), 95. https://doi.org/10.1071/BT9630095.

Yan, G., Hu, R., Luo, J., Weiss, M., Jiang, H., Mu, X., Xie, D., Zhang, W., 2019. Review of indirect optical measurements of leaf area index: Recent advances, challenges, and perspectives. Agric. For. Meteorol. 265, 390–411. https://doi.org/10.1016/j.agrformet.2018.11.033.

Zhang, G., Ren, W., Xu, F., 2009. Curve representation and matching based on feature points and minimal area. J. Comput. Appl. 29 https://doi.org/10.3724/sp.j.1087.2009.01159.

Zou, J., Zhong, P., Hou, W., Zuo, Y., Leng, P., 2020. Estimating Needle and Shoot Inclination Angle Distributions and Projection Functions in Five Larix principis-rupprechtii Plots via Leveled Digital Camera Photography. Forests 12, 30. https://doi.org/10.3390/f12010030.

Zou, X., Mõttus, M., Tammeorg, P., Torres, C.L., Takala, T., Pisek, J., Mäkelä, P., Stoddard, F.L.L., Pellikka, P., 2014. Photographic measurement of leaf angles in field crops. Agric. For. Meteorol. 184, 137–146. https://doi.org/10.1016/j.agrformet.2013.09.010.